EFFECT OF GAS-PHASE REYNOLDS NUMBER ON GAS-LIQUID MASS TRANSFER IN A TURBULENT AIR–WATER CHANNEL FLOW

Adharsh Shankaran & R. Jason Hearst
Department of Energy and Process Engineering
Norwegian University of Science and Technology
Trondheim, 7032, Norway
adharsh.shankaran@ntnu.no, jason.hearst@ntnu.no

ABSTRACT

Gas transfer across the air–water interface is a fundamental process in both natural and engineered systems, yet its dependence on wind-driven turbulence requires further experimental evidence. This study investigates the effect of the air-side Reynolds number on spatio-temporal oxygen dissolution in a wind-sheared air–water channel. Aerodynamic forcing and water-side hydrodynamics are characterized using Particle Image Velocimetry (PIV), matched with simultaneous aqueous Laser-Induced Fluorescence (LIF) to capture dissolved oxygen (DO) concentration fields and interfacial deformation. As the bulk air velocity increases, the onset of capillary-gravity waves acts as dynamic surface roughness, extracting momentum from the airflow. This intensifies the Reynolds shear stress immediately above the interface and induces strong subsurface shear in the aqueous phase. These coupled interactions lead to a nonlinear enhancement in gas transfer velocity (k) of over 600%, with values rising from 3.54 cm/h at centerline velocity $U_c = 4.58$ m/s to 22.56 cm/h at $U_c = 8.96$ m/s. Spatial analysis confirms that the turbulent vertical scalar flux peaks immediately adjacent to the deforming boundary. Furthermore, increasing the air Reynolds number amplifies both localized concentration fluctuations and the net downward oxygen flux, providing direct experimental confirmation that as wind speed increases, wave-induced velocity fluctuations and interfacial deformation accelerate the net turbulent transport of dissolved gases away from the interface.

INTRODUCTION

Gas transfer across the air–water interface is a fundamental process in both natural and engineered systems. Understanding gas transfer at the ocean surface is critical, as the ocean is the largest carbon dioxide sink on the planet and strongly influences climate dynamics (Bunsen *et al.*, 2024). In engineered contexts, such as wastewater treatment and bioreactor aeration, optimizing gas exchange is essential for maintaining dissolved oxygen (DO) levels and operational efficiency (Gabelle *et al.*, 2011).

At the fundamental level, the rate of gas exchange is constrained by a thin diffusive boundary layer at the interface; consequently, the transfer velocity (k) is largely determined by the transport of fluid from the bulk to the surface via turbulent motions. A number of theoretical frameworks have been developed to explain the mechanisms driving this interfacial renewal. Classical Surface Renewal Models (SRM) attribute the exchange to the periodic replacement of interfacial fluid by large-scale bulk eddies (Higbie, 1935; Danckwerts, 1951; Fortescue & Pearson, 1967). In contrast, the Small Eddy Model (SEM) argues that k is governed primarily by the smallest scales of turbulence and the local dissipation rate (Banerjee *et al.*, 1968; Lamont & Scott, 1970). To account for the mobile, deforming interfaces typical of wind-driven flows, the Surface Divergence Model (SDM) was proposed, which links the transfer rate directly to the kinematics of surface stretching and divergence (McCready *et al.*, 1986). More recent investigations, such as those by Turney & Banerjee (2013), demonstrate that a combined SRM-SDM framework can effectively capture these coupled dynamics; however, a single universally applicable model for all flow regimes remains elusive.

Applying these models to wind-driven regimes is difficult due to the non-linear coupling between aerodynamic forcing and subsurface turbulence. Early measurements established that gas transfer is not a simple function of wind speed. At the ocean scale, gas transfer exhibits an approximately quadratic relationship with wind speed (Wanninkhof *et al.*, 2009). However, wind-tunnel experiments by Jähne *et al.* (1979) demonstrated that transfer rates also depend heavily on the wave spectrum, exhibiting an abrupt increase with the onset of rough surface waves. This enhancement is driven by air-side aerodynamics; for instance, Buckley & Veron (2019) utilized air-side PIV and LIF to show that wind-generated waves induce flow separation, spatial stress variations, and boundary layer fluctuations over wave crests. These fluctuations in the air-side shear stress directly modulate the turbulent kinetic energy available for renewal processes in the aqueous phase. On the water side, laboratory studies have sought to isolate these mechanisms. Herlina & Jirka (2004) demonstrated that turbulent mixing alone significantly enhances oxygen transport, while Bullee *et al.* (2024) and Li *et al.* (2025) showed that small-scale turbulence exerts a stronger influence on gas transfer than the interfacial area changes caused by capillary waves. These findings reinforce that turbulence-driven interfacial renewal plays the primary role in controlling transfer velocities (Jähne & Haußecker, 1998; Turney & Banerjee, 2013).While turbulence-driven interfacial renewal is considered the primary driver of gas transfer in the absence of breaking (Jähne & Haußecker, 1998; Turney & Banerjee, 2013), the onset of wave breaking introduces additional complex mechanisms. As highlighted by Deike (2022), bubble-mediated exchange and surface whitecaps significantly enhance the transfer velocity at high sea states, a regime distinct from the shear-driven transport investigated here.

A major bottleneck in validating these coupled dynamics

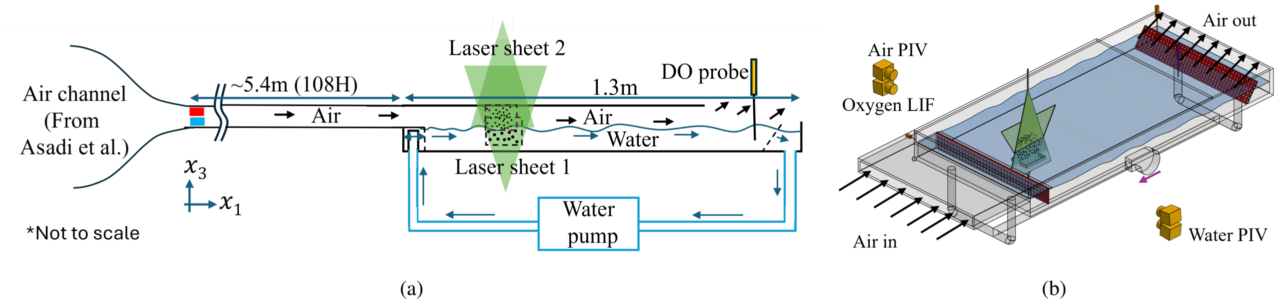

Figure 1: (a) Schematic of the air channel along with the air-water channel. (b) A three-dimensional view of the air-water channel along with the measurement setup.

is the difficulty of simultaneously characterizing the aerodynamic forcing, interfacial deformation, and the resulting turbulent scalar fluxes. Traditional DO measurements using point probes (Sanjou, 2020) or non-instantaneous methods (Turney & Banerjee, 2013) lack the spatial resolution to resolve the thin concentration sub-layer and fail to capture key spatio-temporal dynamics. While Herlina & Jirka (2008) pioneered simultaneous measurements of velocity and DO concentration in a grid-stirred tank, their study was limited to flows without mean velocity and flat interfaces. Building on this, Shankaran & Hearst (2025) measured the spatial and temporal evolution of DO concentration, fluctuations, and flux in an air–water channel using PIV and LIF, providing a framework for resolving gas transfer across deforming interfaces.

The present study extends this framework to investigate the effect of the air Reynolds number on the coupling between air-side shear, interfacial deformation, and water-side oxygen transfer. By performing high-resolution, velocity measurements matched with simultaneous aqueous LIF, we construct a continuous profile of momentum transfer across the air–water boundary. This approach allows us to quantify how fluctuations in air-side Reynolds shear stress directly penetrate the interface to modulate water-side turbulent kinetic energy, ultimately elucidating the physical mechanisms governing gas exchange under wind-driven conditions.

EXPERIMENTAL METHODS

Experiments were conducted in an acrylic air–water channel flow facility measuring 1300 mm in length, 600 mm in width, and 106 mm in height, as shown in Fig. 1(b). To ensure fully developed aerodynamic forcing, this test section is positioned downstream of a 5425 mm long air channel of the same width and a height of 50 mm (H_a) (Asadi *et al.*, 2022). This allows the turbulent airflow to develop over $108H_a$ before interacting with the water surface (Fig. 1(a), ensuring the first- and second-order statistics of the airflow achieve a self-similar, well-developed turbulent state. The air–water channel was filled with water to a depth of 50 mm (H_w), leaving the remaining height for the airflow. A low-rate water pump gently circulated the fluid to prevent the settling of seeding particles without disturbing the interfacial boundary conditions.

To characterize the aerodynamic forcing, velocity measurements in the air phase were conducted using Particle Image Velocimetry (PIV). The air was seeded with water-based smoke, and images were acquired at 15 Hz using an sCMOS camera (2560×2160 pixels) operating in dual-frame mode. Crucially, these air-side measurements were conducted as an independent campaign, with the wind-forcing conditions rigorously matched to the water-side experiments via the bulk air Reynolds number. This approach enables the construction of continuous statistical profiles of momentum transfer across the interface over the tested wind-speed range.

To capture the coupled dynamics of water-side turbulence, DO transfer, and interfacial deformation, simultaneous PIV and Laser-Induced Fluorescence (LIF) measurements were performed in the aqueous phase. Optical access was provided through a quartz glass window located at the bottom of the channel, $5.5H_a$ downstream of the initial air–water interaction region. Illumination was provided by a co-located Litron Nd:YAG laser system emitting simultaneously at 532 nm (visible green) for PIV and 266 nm (UV) for LIF. The water was seeded with 20 μm polystyrene particles for velocity tracking, while an O_2-sensitive dye (1-Pyrene Butyric Acid) was dissolved in the water for DO mapping and surface profiling.

The resulting optical signals were recorded simultaneously by three synchronized sCMOS cameras at 0.5–1 Hz, depending on wind velocity. In-situ calibration of the oxygen LIF signal was performed using a high-resolution DO point probe located within the bulk fluid, allowing the fluorescent intensity fields to be mapped to absolute oxygen concentrations. All PIV data were processed using LaVision DaVis 10.2 via a multi-pass cross-correlation algorithm, yielding a final interrogation window of 32×32 pixels with 50% overlap. The DO processing and calibration followed the rigorous methodology outlined by Shankaran & Hearst (2025). The air–water interface was accurately identified by binarization of LIF images. By combining these independently phase-resolved datasets, this methodology provides a comprehensive framework for quantifying the mechanisms controlling oxygen uptake at a wind-sheared interface.

FLOW CHARACTERISTICS

The macroscopic features of the two-phase flow establish the baseline conditions for interfacial transfer. Figure 2 presents the mean streamwise velocity profiles of the air phase after interacting with the water surface. At lower wind speeds, the profile is relatively symmetric. However, as the bulk air velocity increases, the profile develops a noticeable asymmetry: the velocity gradient near the water surface ($x_3/H = 0$) becomes markedly steeper than at the top wall. This asymmetry reflects the increased aerodynamic roughness and enhanced momentum extraction driven by the onset of surface waves.

In the aqueous phase, the wind shear drives a strong, shallow, forward-moving boundary layer near the surface. To satisfy mass conservation within the closed water channel loop, this surface current is balanced by a slower, pressure-driven recirculation in the deeper bulk fluid. Table 1 summarizes the aerodynamic operating conditions and global flow properties

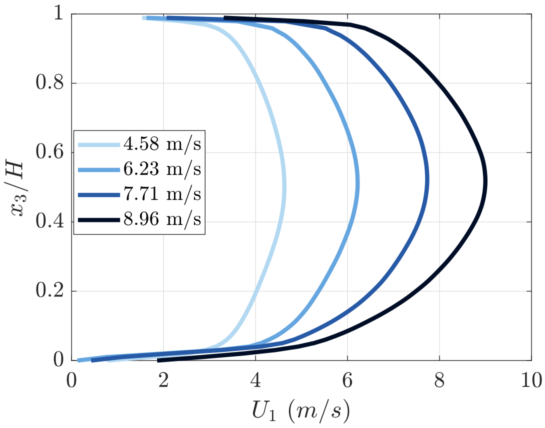

(a)

Figure 2: Mean velocity profile of air flow over the water surface

Table 1: Air velocity and corresponding flow properties

U_c (m/s)	Re_H	U_τ (m/s)	Re_τ
4.58	15400	0.27	442
6.23	20900	0.34	571
7.71	25900	0.42	695
8.96	30100	0.49	804

across the five tested wind speeds, including the centerline air velocity (U_c), the bulk air Reynolds number based on channel height (Re_H), the channel friction velocity (U_τ), and the corresponding friction Reynolds number (Re_τ). The friction velocity was determined directly from pressure drop measurements acquired along the channel length using a pressure scanner (Scanivalve MPS4264).

NEAR INTERFACE DYNAMICS

The turbulent airflow developed over $108H_a$ strongly interacts with the water surface, inducing interfacial deformations that fundamentally modify the shear distribution in both phases. Table 2 summarizes the local near-interface flow properties, including the air-side and water-side friction velocities ($U_{\tau,\mathrm{a}}$, $U_{\tau,\mathrm{w}}$), the mean-square surface slope ($\langle(\nabla\eta)^2\rangle$) where $\nabla = \partial/\partial x_1$ and η is the interface deformation, and the global gas transfer velocity (k). The friction velocities characterizing the interface are estimated as the peak in $(-\overline{u_1' u_3'})^{1/2}$ within the near-interface region, where $\overline{(\cdot)}$ represents the ensemble average (Schultz & Flack, 2007).

Figure 3(a) illustrates the vertical distribution of the dynamic Reynolds shear stress ($\rho\overline{u_1' u_3'}$) across the air–water interface for varying centerline velocities. As the centerline air velocity increases from 4.58 m/s to 8.96 m/s, a profound enhancement in the absolute magnitude of the turbulent stress is observed in both phases. On the air side ($x_3/H > 0$), the intensification of the momentum flux is most prominent immediately above the interface. This highly localized peak is driven by increased aerodynamic drag as the water surface deforms into wind-generated capillary-gravity waves, as visualized in the instantaneous interface snapshots in Figure 3(b).

Table 2: Flow properties near interface.

U_c	$U_{\tau,\mathrm{a}}$ (m/s)	$U_{\tau,\mathrm{w}}$ (m/s)	$\langle(\nabla\eta)^2\rangle$	k (cm/h)
4.58	0.22	0.004	0.021	3.54
6.23	0.33	0.0057	0.044	8.27
7.71	0.48	0.0116	0.065	17.63
8.96	0.57	0.0157	0.079	22.56

The aerodynamic impact of these waves is quantified in Figure 3(c), which presents the air-side boundary layer profiles in inner scaling. At the lowest wind speed (4.58 m/s), the interface is nearly flat ($\langle(\nabla\eta)^2\rangle = 0.021$), and the raw velocity profile closely follows the smooth-wall DNS results of Graham *et al.* (2016). As the wind speed and surface slope increase, the developing waves act as dynamic roughness elements, extracting momentum from the airflow and necessitating a rough-wall correction (Geva & Shemer, 2022). Under these conditions, the mean flow is described by the rough-wall log-law: $U_1^+ = \frac{1}{\kappa}\ln x_3^+ + B - \Delta U_1^+$, where ΔU_1^+ represents the velocity deficit due to surface roughness. To demonstrate this scaling in Fig. 3(c), the profiles for higher wind speeds are shifted upward by their respective ΔU_1^+ values to collapse onto the DNS baseline.

This extracted momentum is conserved across the boundary. As seen in the lower half of Figure 3(a) ($x_3/H < 0$), the amplified dynamic stress on the air side induces a severe, corresponding increase in the sub-surface dynamic Reynolds stress. This mirrored stress profile demonstrates strong interfacial coupling, highlighting how the wave-induced aerodynamic drag results in a substantial enhancement of the absolute downward momentum flux into the water column. This intense, near-surface water-side shear provides the turbulent kinetic energy necessary for the interfacial renewal processes that govern the gas transfer rates reported in Table 2.

BULK DISSOLVED OXYGEN CHARACTERISTICS

The physical consequences of the enhanced near-surface momentum transfer are directly evident in the bulk dissolved oxygen (DO) measurements presented in Figure 4. At the lowest wind speed (4.58 m/s), the water column requires more than 4 hours to reach 95% oxygen saturation. Conversely, at the highest wind speed (8.96 m/s), the intense wave-induced turbulence drives rapid interfacial renewal, achieving near-saturation in under 1.5 hours.

The temporal evolution of the bulk DO concentration, $C(t)$, can be modeled by the first-order relation $C(t)/C_s = 1 - e^{-k_L t}$, where C_s is the saturation concentration and k_L is the volumetric mass transfer coefficient (in units of time^{-1}). To quantify this enhancement, the logarithmic concentration deficit, $\ln(1 - C/C_s)$, is plotted against time in the inset of Figure 4. The magnitude of the slope of the linear fit directly yields k_L. The global gas transfer velocity, k, is then calculated using the relation $k = k_L(V/A)$, where V is the bulk water volume and A is the planar interfacial area.

As reported in Table 2, the coupling between the aerodynamic forcing and the water-side turbulence is highly nonlinear. While doubling the centerline air velocity (from 4.58 m/s to 8.96 m/s) roughly doubles the $U_{\tau,\mathrm{a}}$, it results in an extraordinary 637% increase in the gas transfer velocity, k. This mas-

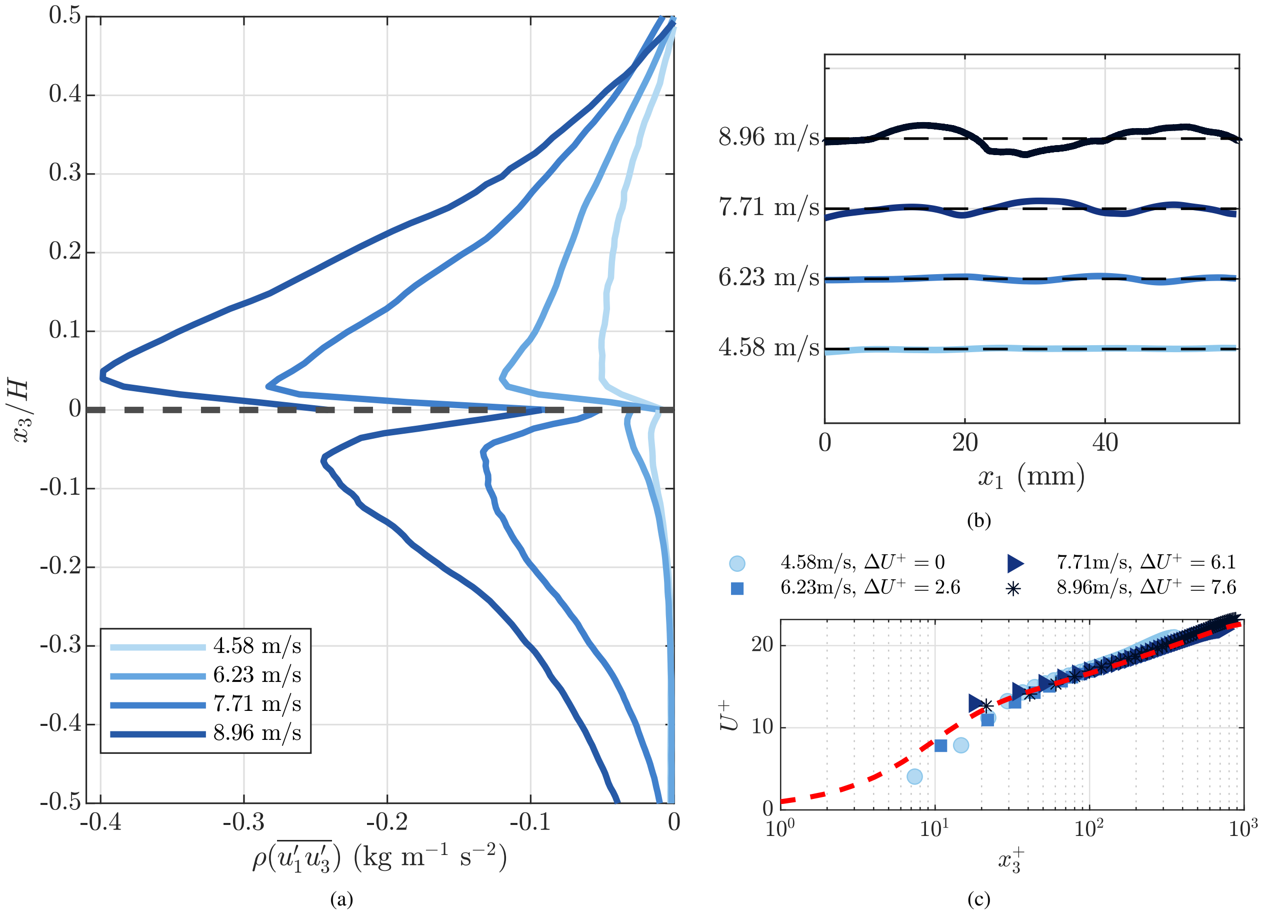

Figure 3: (a) Dynamic Reynolds shear stress ($\rho\overline{u_1'u_3'}$) across air–water interface, where $x_3/H > 0$ is Reynolds shear stress on the air side, $x_3/H < 0$ is Reynolds shear stress on the water side. The ρ used here is the respective density of the fluid. Here, x_1 and x_3 denote the streamwise and wall-normal directions, respectively, while u_1' and u_3' represent the corresponding velocity fluctuations; (b) Instantaneous snapshots of the air–water interface deformation at increasing air velocity. (c) Air-side boundary layer indicating the log region. - - is from DNS study by Graham *et al.* (2016) for smooth wall channel flow with $\mathrm{Re}_\tau = 1000$;

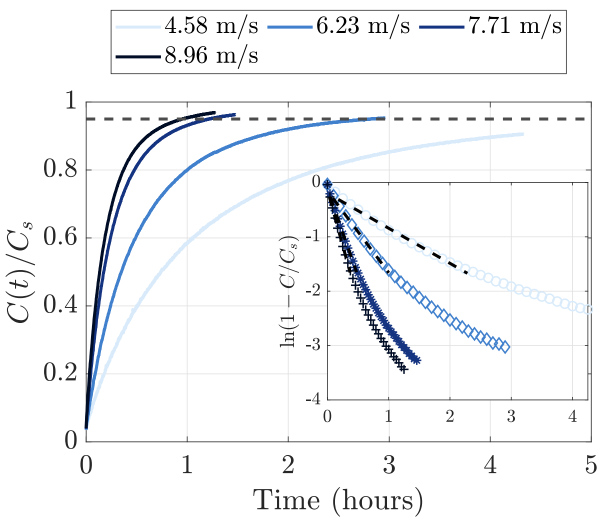

Figure 4: Bulk dissolved oxygen (DO) concentration variation over time (dashed line indicates 95% DO saturation). In the inset log plot, dashed lines represent the linear fit. The slope of these fits is used to calculate the gas transfer velocity, k.

sive enhancement underscores the dominance of wave-induced roughness and small-scale shear in overcoming the diffusive barrier at the interface.

SPATIO-TEMPORAL DISSOLVED OXYGEN CHARACTERISTICS

While bulk measurements confirm an overall enhancement in gas transfer, simultaneous measurements of the aqueous velocity, DO concentration, and surface deformation elucidate the specific transport mechanisms. Figure 5 presents an instantaneous temporal sequence of the velocity vector field overlaid on the DO concentration field at a wind speed of 4.58 m/s. The continuous generation of oxygen at the boundary creates a thin, highly concentrated diffusive sub-layer immediately below the interface.

The visualizations clearly capture the localized, transient nature of the "surface renewal" process. In Figures 5(a) and (d), distinct sweep events are visible, where shear-driven downward velocity fluctuations detach parcels of oxygen-rich fluid from the interfacial sub-layer and transport them deep into the bulk fluid. Conversely, Figure 5(b) illustrates the entrainment of this oxygen-rich fluid into a coherent vortex structure. These coherent turbulent motions physically strip the saturated fluid from the boundary, thinning the local concentra-

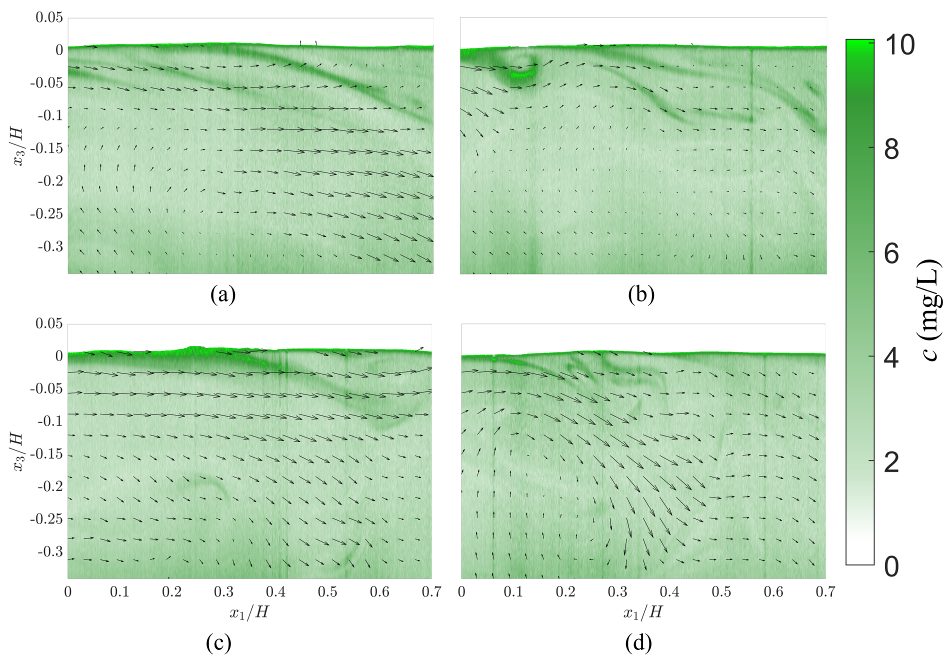

Figure 5: Instantaneous water velocity vector fields overlaid on the dissolved oxygen (DO) concentration field, showing snapshots acquired at 1 Hz. The air velocity is 4.58 m/s, generating low-amplitude interfacial waves. Regions of high intensity (green) indicate elevated DO concentration relative to the surrounding fluid.

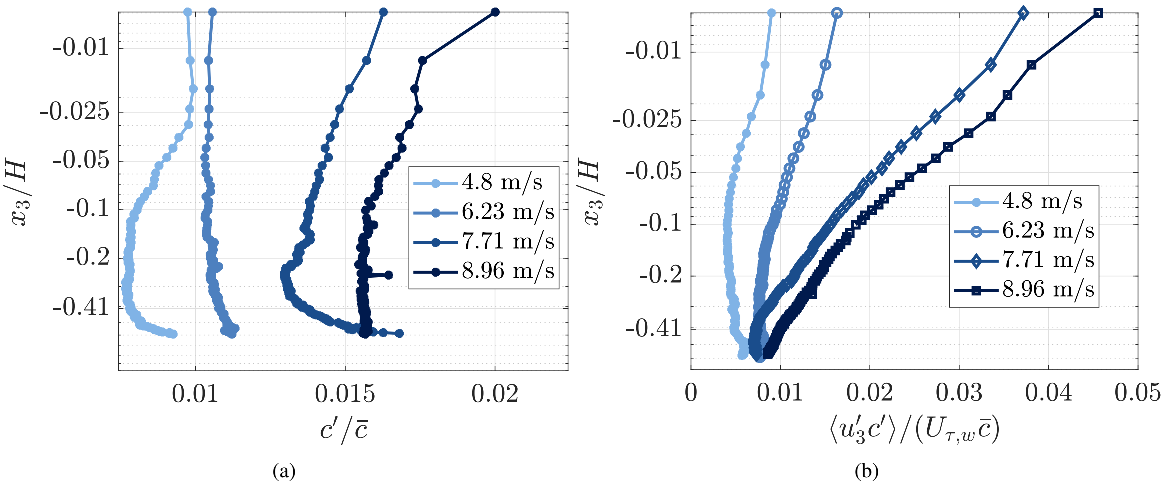

Figure 6: (a) Concentration fluctuation for various air velocities with $\bar{c} = 0.9$; (b) Vertical concentration flux for various air velocities with $\bar{c} = 0.9$

tion sub-layer and maintaining the sharp concentration gradients necessary to drive further gas absorption.

To quantify these turbulent transport mechanisms across the range of wind forcing, we analyze the concentration statistics at a matched bulk saturation state ($\bar{c}/C_s \approx 0.9$). As demonstrated in our previous work (Shankaran & Hearst, 2025), concentration fluctuations and turbulent fluxes are strongly dependent on the transient bulk saturation level. By isolating our analysis to this near-saturation regime, where the bulk concentration deficit is constrained to approximately 10%, we mimic the realistic, quasi-steady state of typical natural ocean surfaces. Figure 6(a) presents the vertical profiles of the root-mean-square (RMS) concentration fluctuations, normalized by the local mean concentration ($c'/\bar{c}$). The profiles reveal a consistent structural feature across all wind speeds: the fluctuation intensity remains nearly constant close to the interface due to intense shear-driven homogenization, but increases deeper into the channel as discrete packets of highly concentrated fluid mix with the lower-concentration bulk. Furthermore, as the air velocity increases and the interface transitions from flat to wave-roughened, the absolute magnitude of these scalar fluctuations increases significantly. This amplification confirms that the enhanced aerodynamic wave-drag directly injects higher-intensity turbulent energy into the aqueous concentration boundary layer.

The net effect of these fluctuations on the actual mass transport is captured by the turbulent vertical scalar flux, $\langle u_3' c' \rangle$. Figure 6(b) displays the vertical flux profiles, normalized by the water-side friction velocity and the mean concentration ($U_{\tau,w}\bar{c}$). The downward transport of oxygen is heavily localized in the near-surface region. Crucially, the magnitude of this turbulent flux increases monotonically with wind speed. The most dramatic enhancement occurs between the low-wind, smooth-interface regime (4.58 m/s) and the high-wind, rough-interface regimes (7.71 m/s and 8.96 m/s). This scaling provides direct experimental confirmation that as wind speed increases, vertical velocity fluctuations and interfacial deformation dramatically accelerate the net turbulent transport of dissolved gases away from the interface.

CONCLUSIONS

The spatio-temporal dynamics of oxygen transfer across a wind-driven air–water interface are governed by intricate, multi-scale coupling of aerodynamics, interfacial kinematics, and subsurface turbulence. The current simultaneous measurement allows direct observation of turbulent scalar transport, leading to the following primary conclusions:

- As the bulk air velocity increases, the onset of capillary-gravity waves acts as dynamic surface roughness. This extracts substantial momentum from the airflow, evidenced by a distinct downward shift (ΔU^+) in the logarithmic velocity profile and a highly localized enhancement in the air-side Reynolds shear stress immediately above the wave crests.
- The momentum extracted from the air phase is transferred across the boundary, inducing strong sub-surface Reynolds stresses. This intense, near-surface shear provides the turbulent kinetic energy necessary to drive aqueous mixing.
- Spatio-temporal LIF visualizations and statistical flux profiles ($\langle u_3' c' \rangle$) reveal that interfacial gas transfer is driven by localized, transient sweep events and vortex entrainment. These coherent structures physically strip oxygen-rich fluid from the diffusive sub-layer, transporting it deep into the bulk and maintaining the sharp concentration gradients required for continued absorption.
- The coupling between wind-driven surface deformation and small-scale turbulence results in a highly nonlinear enhancement of the mass transfer rate. Doubling the centerline wind speed (from 4.58 m/s to 8.96 m/s) yielded a 637% increase in the global gas transfer velocity (k).
- Taken together with the recent findings of Li *et al.* (2025), these results suggest that the turbulence induced in the aqueous phase is the primary driver of the transport enhancement, rather than the physical action of the waves themselves.

ACKNOWLEDGMENTS

This work was funded by European Union (ERC, GLITR, 101041000). Views and opinions expressed are, however, those of the authors only and do not necessarily reflect those of the European Union or the European Research Council Executive Agency. Neither the European Union nor the granting authority can be held responsible for them.

REFERENCES

Asadi, M, Kamruzzaman, M & Hearst, R J 2022 The effect of inlet turbulence on the quiescent core of turbulent channel flow. *J. Fluid Mech.* **935**, A37.

Banerjee, S, Scott, DS & Rhodes, E 1968 Mass transfer to falling wavy liquid films in turbulent flow. *Ind. Eng. Chem. Fundam.* **7** (1), 22–27.

Buckley, M P & Veron, F 2019 The turbulent airflow over wind generated surface waves. *Eur. J. Mech. B/Fluids* **73**, 132–143.

Bullee, P A, Weichert, S, Nore, A, Li, L, Ellingsen, S Å & Hearst, R J 2024 The influence of water turbulence on surface deformations and the gas transfer rate across an air–water interface. *Exp. Fluids* **65** (9), 132.

Bunsen, F, Nissen, C & Hauck, J 2024 The impact of recent climate change on the global ocean carbon sink. *Geophys. Res. Lett.* **51** (4), e2023GL107030.

Danckwerts, P V 1951 Significance of liquid-film coefficients in gas absorption. *Ind. Eng. Chem.* **43** (6), 1460–1467.

Deike, L 2022 Mass transfer at the ocean–atmosphere interface: the role of wave breaking, droplets, and bubbles. *Annu. Rev. Fluid Mech.* **54** (1), 191–224.

Fortescue, GE & Pearson, JRA 1967 On gas absorption into a turbulent liquid. *Chem. Eng. Sci.* **22** (9), 1163–1176.

Gabelle, JC, Augier, F, Carvalho, A, Rousset, R & Morchain, Jérôme 2011 Effect of tank size on $k_{\mathrm{L}}a$ and mixing time in aerated stirred reactors with non-Newtonian fluids. *Can. J. of Chem. Eng.* **89** (5), 1139–1153.

Geva, M & Shemer, L 2022 Wall similarity in turbulent boundary layers over wind waves. *J. Fluid Mech.* **935**, A42.

Graham, J, Kanov, K, Yang, XIA, Lee, M, Malaya, N, Lalescu, CC, Burns, R, Eyink, G, Szalay, A, Moser, RD *et al.* 2016 A web services accessible database of turbulent channel flow and its use for testing a new integral wall model for LES. *J. Turbul.* **17** (2), 181–215.

Herlina & Jirka, GH 2008 Experiments on gas transfer at the air–water interface induced by oscillating grid turbulence. *J. Fluid Mech.* **594**, 183–208.

Herlina & Jirka, G H. 2004 Application of lif to investigate gas transfer near the air–water interface in a grid-stirred tank. *Exp. Fluids* **37**, 341–349.

Higbie, R 1935 The rate of absorption of pure gas into a still liquid during short periods of exposure. *Trans. Am. Inst. Chem. Engrs.* **31**, 365–389.

Jähne, B & Haußecker, H 1998 Air-water gas exchange. *Annu. Rev. Fluid Mech.* **30** (1), 443–468.

Jähne, B, Münnich, KO & Siegenthaler, U 1979 Measurements of gas exchange and momentum transfer in a circular wind-water tunnel. *Tellus* **31** (4), 321–329.

Lamont, John C & Scott, DS 1970 An eddy cell model of mass transfer into the surface of a turbulent liquid. *AIChE J.* **16** (4), 513–519.

Li, L, Bullee, P A, Ellingsen, S Å & Hearst, R J 2025 Sub-surface turbulence or non-breaking capillary waves: which dominates air–water gas transfer? *J. Fluid Mech.* **1009**, A48.

McCready, MJ, Vassiliadou, E & Hanratty, TJ 1986 Computer simulation of turbulent mass transfer at a mobile interface. *AIChE J.* **32** (7), 1108–1115.

Sanjou, M 2020 Local gas transfer rate through the free surface in spatially accelerated open-channel turbulence. *Phys. Fluids* **32** (10).

Schultz, MP & Flack, KA 2007 The rough-wall turbulent boundary layer from the hydraulically smooth to the fully rough regime. *J. Fluid Mech.* **580**, 381–405.

Shankaran, A & Hearst, R J 2025 Simultaneous measurements of velocity, oxygen concentration, and deformed interface position in an air–water channel using PIV and LIF. *Exp. Fluids* **66** (5), 95.

Turney, D E & Banerjee, S 2013 Air–water gas transfer and near-surface motions. *J. Fluid Mech.* **733**, 588–624.

Wanninkhof, R, Asher, W E, Ho, D T, Sweeney, C & McGillis, W R 2009 Advances in quantifying air-sea gas exchange and environmental forcing. *Annu. Rev. Mar. Sci.* **1** (1), 213–244.